

● Original Contribution

A NOVEL ULTRASOUND PROBE SPATIAL CALIBRATION METHOD USING A COMBINED PHANTOM AND STYLUS

TIEXIANG WEN,^{*,†,§,1} CHENG WANG,^{*} YI ZHANG,^{†,1} and SHOUJUN ZHOU^{*,†}

^{*} Shenzhen Institutes of Advanced Technology, Chinese Academy of Sciences, Shenzhen, P. R. China; [†] Center of Interventional Radiology & Vascular Surgery, Department of Radiology, Zhongda Hospital, Medical School, Southeast University, Nanjing, P.R. China; [‡] Key Laboratory of Health Informatics, Chinese Academy of Sciences, Shenzhen, P. R. China; and [§] University of Chinese Academy of Sciences, Beijing, P.R. China

(Received 31 July 2019; revised 6 March 2020; in final form 22 March 2020)

Abstract—Intra-operative ultrasound (US) is a popular imaging modality for its non-radiative and real-time advantages. However, it is still challenging to perform an interventional procedure under two-dimensional (2-D) US image guidance. Accordingly, the trend has been to perform three-dimensional (3-D) US image guidance by equipping the US probe with a spatial position tracking device, which requires accurate probe calibration for determining the spatial position between the B-scan image and the tracked probe. In this report, we propose a novel probe spatial calibration method by developing a calibration phantom combined with the tracking stylus. The calibration phantom is custom-designed to simplify the alignment between the stylus tip and the B-scan image plane. The spatial position of the stylus tip is tracked in real time, and its 2-D image pixel location is extracted and collected simultaneously. Gaussian distribution is used to model the spatial position of the stylus tip and the iterative closest point-based optimization algorithm is used to estimate the spatial transformation that matches these two point sets. Once the probe is calibrated, its trajectory and the B-scan image are collected and used for the volume reconstruction in our freehand 3-D US imaging system. Experimental results demonstrate that the probe calibration approach results in less than 1-mm mean point reconstruction accuracy. It requires less than 5 min for an inexperienced user to complete the probe calibration procedure with minimal training. The mockup test shows that the 3-D images are geometrically correct with 0.28°-angle accuracy and 0.40-mm distance accuracy. (E-mail: sj.zhou@siat.ac.cn) © 2020 The Author(s). Published by Elsevier Inc. on behalf of World Federation for Ultrasound in Medicine & Biology. This is an open access article under the CC BY-NC-ND license. (<http://creativecommons.org/licenses/by-nc-nd/4.0/>).

Key Words: Probe calibration, Calibration phantom, Point clouds registration, 3-D Ultrasound imaging, Ultrasound guidance.

INTRODUCTION

Intra-operative ultrasound (US) is an important and useful imaging modality attributable to its non-radiative, non-invasive, portable and real-time imaging advantages. But conventional two-dimensional (2-D) US image lacks the three-dimensional (3-D) anatomic structure and requires surgeons to visualize the 3-D anatomy from a series of pre-scanned B-scan images (Fenster et al. 2013). It increases the mental burden of surgeons and requires more professional training to complete the 2-D US image-guided interventions. The emerging

freehand 3-D US is gaining recognition in the field of intra-operative imaging applications by displaying 3-D anatomy, volume measurement, surgery planning and fusion imaging guidance (Xia et al. 2017). A freehand 3-D US imaging system consists of a conventional US scanner, a tracking system and a tracked 2-D US probe (Mozaffari and Lee 2017). The position/orientation sensor is integrated into the probe and tracks the scanning trajectory of the probe in real time through the tracking system. As the probe sweeps across the scanned subject, the position and orientation of the probe along with its corresponding B-scan image are recorded simultaneously. These irregular 2-D B-scan slices are then used to assemble (*via* interpolation) 3-D regular volume data. However, the spatial information of the tracked probe is not directly related to the B-scan image plane. It is

Address correspondence to: Shoujun Zhou, 1068 Xueyuan Avenue, Shenzhen University Town, Shenzhen, GD 518055, P.R. China. E-mail: sj.zhou@siat.ac.cn

¹ Tiexiang Wen and Yi Zhang both as equal contributors.

therefore mandatory to obtain the spatial transformation from the 2-D pixel coordinate of the B-scan image to the 3-D coordinate of the tracked probe. Such rigid transformation can be estimated through a procedure referred to as probe calibration. Once the probe is calibrated, the trajectory of the probe is determined, and the B-scan image can be spatially tracked. Accurate probe spatial calibration is crucial to the success of subsequent volume reconstruction and image-guided interventions (Kim et al. 2013).

The procedure of a probe calibration system consists of the following three components (Mercier et al. 2005): the design of a calibration phantom, which is an object with known geometry and designed for B-scan imaging; the extraction of image features, which aims at locating the phantom features in the B-scan image; and the minimization of the calibration equation, which is used to resolve the solution of linear equations for probe calibration. Rapid, accurate and reliable probe calibration depends on the well-designed calibration phantom, which is capable of reducing the operation time and calibration error. A number of phantoms for probe calibration have been reported and evaluated in Mercier et al. (2005) and Hsu et al. (2009). These calibration objects can be grouped into the following two categories: phantom-based calibration and stylus-based calibration.

The basic idea behind the phantom-based calibration is to design a model that meets a specific solution requirement. These categories of phantom can be classified as point-based phantom, wire-based phantom and wall-based phantom (Mercier et al. 2005). The point-based methods attempt to scan a fiducial point formed by a small spherical object or single cross wire (Melvær et al. 2012). The fiducial point is imaged from various viewing angles and segmented in each B-scan image. By considering this point as being the origin of the phantom coordinate system, an over-determined linear system is yielded and solved using an optimization technique. But it is difficult for the user to align the imaging plane of the US probe sharply across the center of the point because of the finite thickness of the US beam forming (Meairs et al. 2000; Kowal et al. 2003; Leotta 2004; Zhang et al. 2018). The N-wire phantoms are composed of multiple wires that are connected as N-shape or Z-shape (Prager et al. 1998; Lindseth et al. 2003; Carbajal et al. 2013; Najafi et al. 2014). The location of the intersection point between the wires and the scan plane is segmented from the B-scan image. It is attractive for the N-wire phantom because it only needs one image and does not require accurate alignment with the scan plane. However, it is difficult to accurately locate the centers of the intersection points because these objects do not appear as clear dots in the B-scan image, but as smeared ellipses. The wall phantoms produce line features in the B-scan image by scanning a flat plane submersed in the

water tank (Najafi et al. 2015). The advantage of this approach is that the line imposes more constraints to the calibration solution. However, it is difficult to segment and fit the line in the B-scan image accurately.

Another type of calibration is stylus based, in which a 3-D localizer locates a point in space. One end of the stylus is connected to another position/orientation sensor, and the other end is a point target, which is aligned and imaged by the scan plane. According to the shape of the tip, the commonly used styluses include the sharp or spherical stylus (e.g., standard Polaris stylus, Northern Digital Inc., Waterloo, ON, Canada), rod stylus (Khamene and Sauer 2005), cone stylus and Cambridge stylus (Hsu et al. 2008). In general, an additional calibration for the stylus itself is required to determine the rigid-body transform between the position/orientation sensor and the stylus tip. This transformation matrix is usually supplied by the manufacturer (Muratore and Galloway 2001) or can be determined by a simple pointer calibration (Leotta et al. 1997a). In any case, the position of the stylus tip is known in space before probe calibration. This simplifies the optimization and allows for a closed-form solution. However, it is difficult to precisely align the stylus tip with the scan plane.

Feature extraction focuses on the segmentation of the phantom feature from the B-scan image, such as identifying wire crossings, points and lines. Generally speaking, it is easier and more reliable to segment lines than points in the B-scan image. To obtain accurate results, wire crossings and points are often manually or semi-automatically segmented from each B-scan image. On the other hand, lines in the B-scan image are often automatically extracted using some robust line detection algorithms, such as the threshold method (Najafi et al. 2014), the random sample consensus method (Prager et al. 1998) and the Hough transform method (Rousseau et al. 2005).

Once the point sets in the B-scan image and point sets of phantom's feature are obtained, the solution of the US probe calibration problem can be determined by resolving the over-determined system of equations. In general, there are two types of minimization approaches, the closed-form (Nelson and Pretorius 1997; Lindseth et al. 2003; Rousseau et al. 2003) and the iterative methods. If the position of the phantom's feature in world space is known during calibration, a closed-form solution can be obtained. Otherwise, the minimization problem of calibration is solved by iterative methods, such as the iterative closest point (ICP) algorithm (Welch et al. 2002), the Hooke-Jeeves algorithm (Bouchet et al. 2001) and the Levenberg-Marquardt algorithm (Moré, 1978).

In this report, we present a novel probe spatial calibration approach to create a freehand 3-D US imaging system for image-guided interventions. The main contributions of this report are twofold. First, we develop an

integrated marker frame for freehand 3-D US imaging. In the US probe, the marker frame with the position/orientation sensor is integrated into the clinical needle-guide. Under the integrated design of the needle-guide with the marker frame, the B-scan image is capable of providing 3-D image guidance for surgical procedures. Second, a new type of calibration phantom combined with the stylus is proposed. The custom-designed phantom ensures the alignment between the probe scan plane and the stylus tip, which guarantee the accurate localization and detection for the stylus tip in the B-scan image. The ICP-based optimization, which does not require the one-to-one correspondences between two point sets and enables an inexperienced user to perform the accurate probe calibration.

MATERIALS AND METHODS

The materials in our experimental design are the 4.5-MHz abdominal curvilinear transducer (C5-2 E, Mindray Medical International Ltd., Shenzhen, Guangdong, China) and the corresponding US scanner (DC7, Mindray Medical International Ltd.). The conventional 2-D US probe was instrumented with a clinical needle-guide (NCB-015, Mindray Medical International Ltd.), which has a side slot for performing the procedure of needle placement, as presented in [Figure 1a](#). To track the spatial position of the US probe, we have developed a marker frame integrated with the passive optical spheres, as presented in [Figure 1b](#). The marker frame is integrated into the clinical needle-guide and real-time tracked by the optical tracking system (Polaris Spectra, NDI, Ontario, Canada). With the needle-guide integrated with marker frame ([Fig. 1c](#)), the US probe is spatially tracked, and the positioning data are transmitted to our custom-designed software system through an RS232 serial port with the baud rate of 9600 bits/s. Once the probe is

calibrated, the B-scans image is spatially located and acquired by the freehand 3-D US imaging system ([Wen et al. 2018](#)). For this, the US probe spatial calibration plays an important role in determining the accuracy of volume reconstruction (described in the next section of this report).

The US probe spatial calibration system

With the aim of performing an easy, rapid and reliable probe calibration, we have designed a calibration system based on both calibration phantom and stylus. [Figure 2a](#) presents the calibration system setup, which includes a US probe with a position/orientation sensor, a custom-designed phantom and a positioning stylus. The tracked US probe is fixed above the top of the phantom, and the tracked stylus is inserted into the side holes of the phantom. The calibration phantom is designed to ensure that the stylus tip ends up at the US imaging plane in the phantom. For this, the probe is equipped with a needle-guide, and a calibration needle (18-Ga \times 200-mm trocar needle with an asymmetric sharp point) is inserted into the slot of the phantom through the guide. The co-planar relationship between the needle tip and the stylus tip was validated by verifying the intersection point between the needle tip and stylus tip in the B-scan image, as presented in [Figure 2b](#).

Under this system setup, [Figure 2c](#) illustrates the relationship among these coordinate systems, which consist of the image coordinate system I , the position/orientation sensor coordinate system S and the world coordinate system W (*i.e.*, the optical tracking system). We use the stylus tip to directly measure the spatial position of intersection point in 3-D space by pointing the stylus at the target in our calibration system. Because the stylus tip coincides with the center of the phantom slot, it coincides with the US B-scan image plane. The pixel

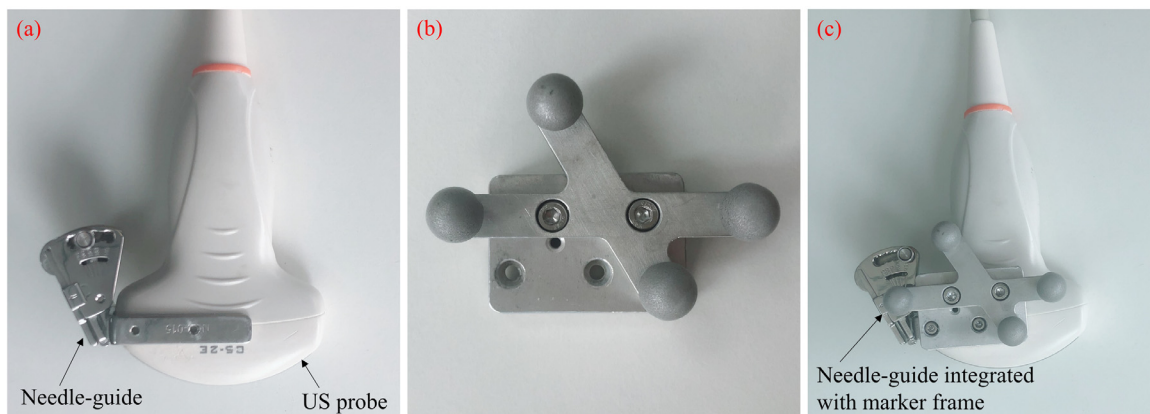


Fig. 1. The integrated needle-guide for US probe tracking. (a) Conventional needle-guide on the US probe. (b) The developed marker frame with passive optical spheres. (c) The needle-guide integrated with marker frame for 3-D spatial positioning.

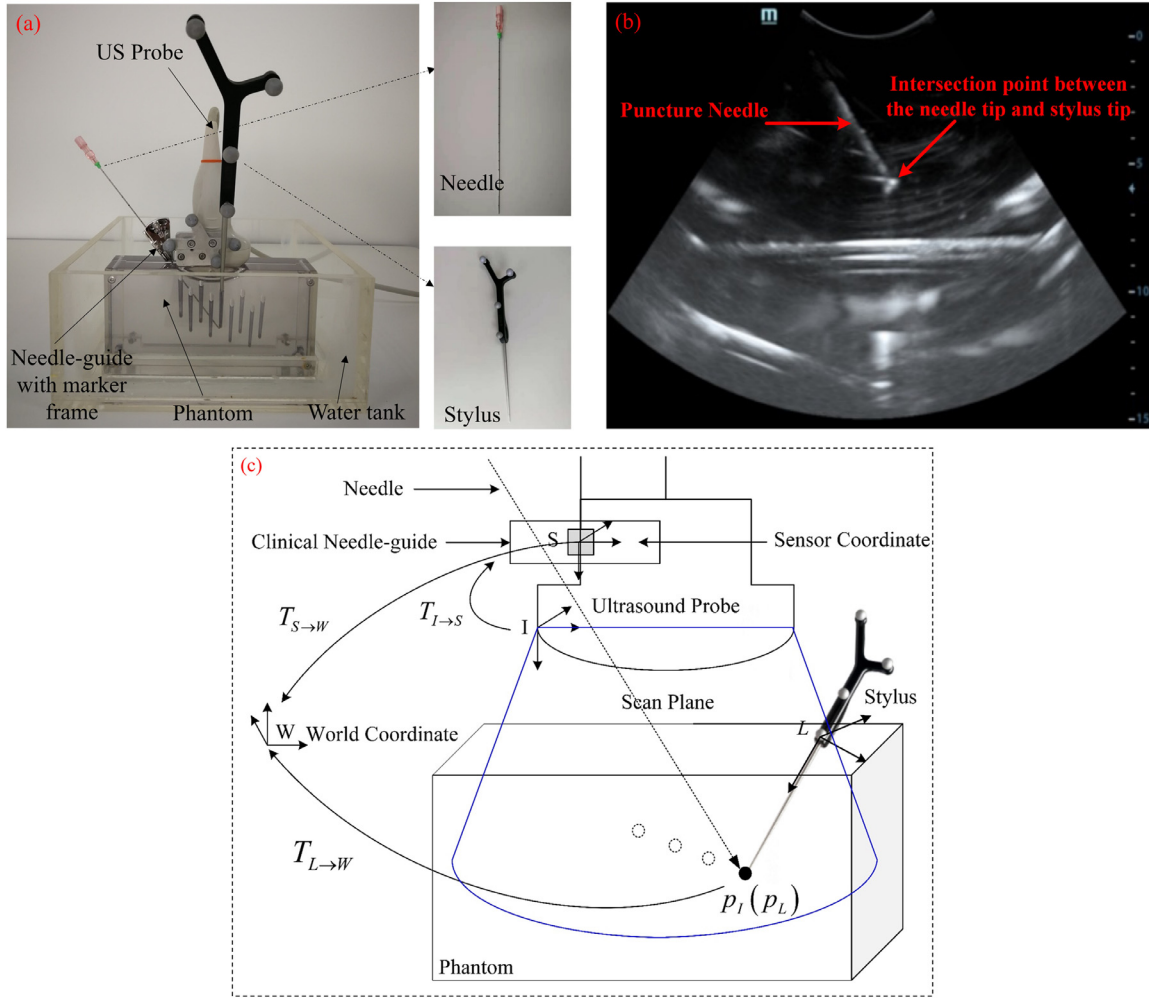


Fig. 2. The US probe spatial calibration system setup. (a) The system setup including the calibration phantom, stylus, US probe with position/orientation sensor and the clinical needle. (b) The co-planar relationship validation between the needle tip and the stylus tip. (c) The coordinate associated with the calibration system.

location p_I of the stylus tip in the B-scan image is transformed to the world coordinate as follows (Melvær et al. 2012):

$$p_W = T_{S \rightarrow W} \cdot T_{I \rightarrow S} \cdot p_I, \text{ with } p_I = \begin{bmatrix} s_x \cdot u & s_y \cdot v & 0 & 1 \end{bmatrix}^T \quad (1)$$

where p_W is the position of the feature point in the world coordinate system; (u, v) is the 2-D pixel coordinate in the B-scan image coordinate system I ; s_x and s_y are the scaling factors representing the pixel spatial resolution along the x and y direction, respectively; p_I is the homogeneous physical coordinate of the pixel; p_P is the 3-D spatial location for the feature point at pixel position p_I ; $T_{I \rightarrow S}$ is the unknown rigid transformation from B-scan image to position/orientation sensor coordinates S and

$T_{S \rightarrow W}$ denotes the rigid transformation from position/orientation sensor to the world coordinates W .

The image feature point at location (u, v) is extracted by the semi-automatic method in our system. In general, we have the isotropic scaling factors (*i.e.*, $s_x = s_y$ for the B-scan image). The image to the position/orientation sensor transformation $T_{I \rightarrow S}$ is determined by probe calibration. The sensor to world transformation $T_{S \rightarrow W}$ is read and updated in real time by the tracking system, which is fixed in relation to the phantom and is used as the origin of the world coordinate. In our combined approach, the position p_W of the feature point is measured directly by the stylus tip.

Under the coordinate configuration, the data sets of p_I , p_W and $T_{S \rightarrow W}$ are collected in our system. Given these data sets, the US probe calibration is performed to estimate the spatial transformation $T_{I \rightarrow S}$

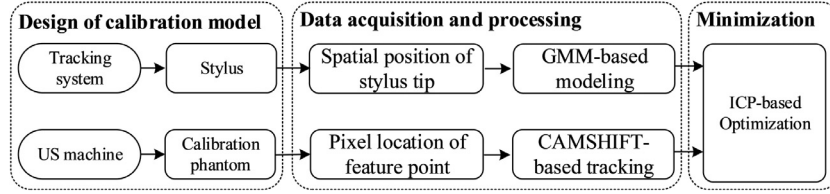


Fig. 3. Workflow of our probe calibration framework.

$$\min \sum \| p_W - T_{S \rightarrow W} \cdot T_{I \rightarrow S} \cdot p_I \|^2 \quad (2)$$

In general, our probe calibration framework consists of three components (see Fig. 3): the design of the calibration model, the customized data acquisition and processing system and the optimization of the probe calibration. We describe in detail each component of the framework in the next sections of this report.

The design of the calibration phantom and stylus

Our designed calibration model includes a custom-designed phantom and a positioning stylus, as illustrated in Figure 4a. The calibration phantom is made of plexi-glass with the dimension of 20 cm × 10 cm × 5 cm. The US probe is clipped firmly with the bolts above the U-shape notch of the calibration phantom. The slot in the center of the phantom is filled with water when the phantom is submersed into the water tank. To overcome the beam thickness problem, the phantom is designed to fix the probe in such a way that the center of the B-scan imaging plane passes through the center of the phantom slot (Fig. 4b). There are nine holes, which are drilled into the slot from one side of the phantom. The size of these holes is designed according to the shape of the positioning stylus, and the holes are used for the

placement of the stylus (Fig. 4c). The stylus tip coincides with the center of the slot so that it coincides with the B-scan imaging plane. Meanwhile, it provides in each B-scan image with a strong, bright echo spot, which can be semi-automatically detected with high accuracy. It facilitates the calibration procedure and data collection.

The stylus is often referred to as the pointer or 3-D localizer, which can be used to obtain the location of any point in 3-D space by pointing the stylus at the target. On one end, the stylus has been attached a position/orientation sensor that can be tracked by the tracking system. On the other end, its tip is sharpened to a point whose location in 3-D space may be supplied by the manufacturer or can be determined by a pointer calibration (Hsu *et al.* 2008). Figure 5a illustrates the coordinate system for the stylus. Suppose that p_L is the position of its tip in the stylus's coordinate system L and $T_{L \rightarrow W}$ is the rigid-body transformation from stylus's coordinate L to world coordinate W , then the position of the stylus tip in world coordinate system is given by

$$p_W = T_{L \rightarrow W} \cdot p_L \quad (3)$$

To perform the pointer calibration, the stylus tip is first placed in the divot, whose size and shape match the tip size and shape. Then we pivot the stylus in a cone shape, at an angle of 30° to 60° from the vertical, as illustrated in Figure 5b. During the tool tip calibration, we need to

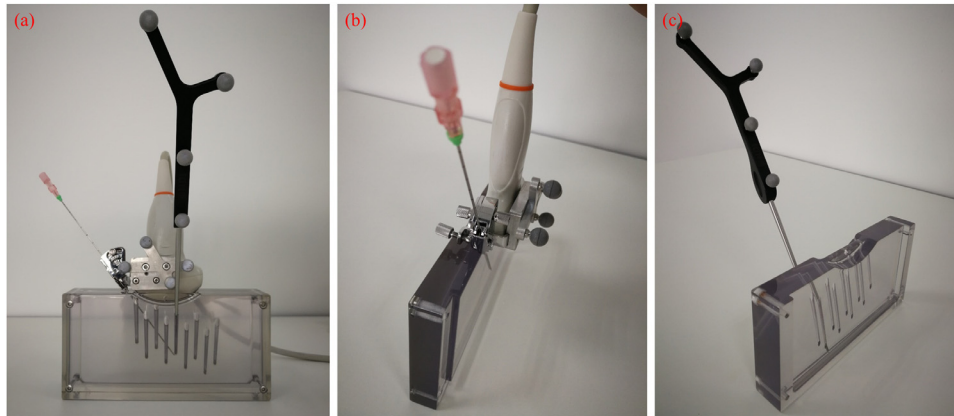


Fig. 4. The designed calibration model and both side views, presenting the inner structure for needle and stylus placement, respectively. (a) The designed calibration model. (b) One inner side view of the phantom for needle placement. (c) Another inner side view of the phantom for stylus placement.

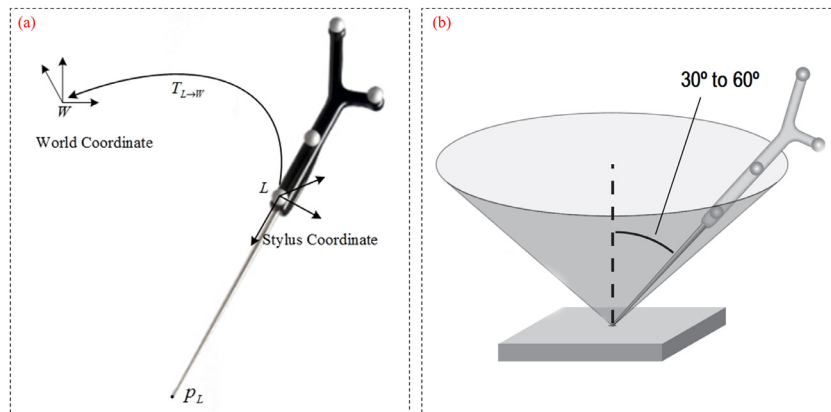


Fig. 5. The stylus coordinate and its calibration. (a) The Polaris-type stylus coordinate system. (b) The stylus calibration using pivoting technique.

collect various poses of the stylus by rotating the instrument in a slow and smooth motion. If the angle for stylus calibration is narrow (e.g., $<30^\circ$), the collected pose data may not be variable enough and result in the increase of calibration error. On the other hand, if the angle for stylus calibration is wide (e.g., $>60^\circ$), the stylus tip could not be easily fixed in the divot and may cause calibration error during data acquisition. Because the stylus tip remains stationary throughout the pivoting procedure, its location p_W in the world coordinate system is therefore fixed. Then the position p_L of the stylus tip can be solved by minimizing the following equation:

$$\min \sum_i \| \overline{p_W^i} T_{L \rightarrow W}^i \cdot p_L^2 \| \quad (4)$$

where $\overline{p_W^i}$ and $T_{L \rightarrow W}^i$ are the position/orientation sensor's reading during the pointer calibration. During the pivoting procedure in our experiment, we pivoted the stylus slowly and smoothly in at a minimum of 2 directions, for approximately 20 s, at an angle of 30° to 60° from the vertical. The root mean square errors for the stylus calibration was 0.18 mm.

In general, the procedure of US probe calibration is described as follows: first, the phantom is submersed in the water tank. The tracked US probe is placed over the notch of the phantom. The stylus is inserted into the holes of the phantom one-by-one during data acquisition. For each placement of the stylus tip in the phantom, its pixel location and spatial position are collected for a period of time by our custom-designed software system. The data collection over time allows for variability caused by the tracking system or by manual operation. These additional collected data are then used to reduce the final calibration error. The slot in the center of the phantom acts as a virtual plane, which coincides with the US scan plane subjected to the constraints imposed by the custom-designed phantom. The intersection point

between the virtual plane and the stylus tip yields a strong echo spot in the B-scan image, with relatively higher intensity. The position p_L of stylus tip in the B-scan is extracted and semi-automatically tracked and its spatial position p_W is read directly from the optical tracking system. Next, we describe how to detect the pixel location p_L and model the spatial position p_W of stylus tip.

Detection and modeling of stylus tip

For probe calibration, the stylus tip is placed into the hole of the phantom and acts as the feature point in the B-scan image. The pixel location of the feature point in the B-scan is semi-automatically extracted and continuously tracked by the Continuously-Adaptive-Mean-Shift (CAMSHIFT) algorithm (Bradski and Clara 1998) during data acquisition. CAMSHIFT is a computationally efficient object tracking algorithm and is capable of tracking the bright echo spot of the feature point in real time.

The CAMSHIFT-based extraction and tracking of feature points is as follows: first, the user draws a circle around the echo spot of the feature point as the region of interest, which acts as the initial search window for the CAMSHIFT algorithm. The mean location within the search window is then automatically computed and continuously updated based on the mean shift algorithm (Fukunaga and Hostetler 1975). The procedure is continued until required accuracy is met. For each extraction of a feature point, a simple and rough circle drawing of the echo spot is only required, and the CAMSHIFT-based tracking algorithm is capable of reporting the accurate pixel location of the feature point continuously.

During the acquisition of the pixel location of the feature point, the spatial position of the stylus tip in the world coordinate is recorded simultaneously. To better model the behavior of the spatial position data, the

Gaussian mixture model (GMM) is introduced for the density estimation of each feature point. Assuming that the spatial position data of the feature point are independently identically distributed, then its probability density function is a weighted sum of the Gaussian probability and can be expressed as follows:

$$\sum_{i=1}^N \log \left\{ \sum_{k=1}^K \pi_k \cdot \mathcal{N}(x_i | \mu_k, C_k) \right\} \quad (5)$$

where N is the number of the data points, K is the number of clusters, π_k is the weighted factor for cluster k and $\mathcal{N}(x_i | \mu_k, C_k)$ is the Gaussian distribution for data point x_i with the mean value μ_k of and the covariance matrix C_k . According to the expectation-maximization algorithm, the parameters of GMM are estimated as follows:

$$\begin{cases} \gamma(i, k) = \pi_k \cdot \mathcal{N}(x_i | \mu_k, C_k) / \sum_{j=1}^K \pi_j \cdot \mathcal{N}(x_i | \mu_j, C_j) \\ N_k = \sum_{i=1}^N \gamma(i, k), \quad \pi_k = N_k / N \\ \mu_k = \left(\sum_{i=1}^N \gamma(i, k) x_i \right) / N_k \\ C_k = \left(\sum_{i=1}^N \gamma(i, k) (x_i - \mu_k)(x_i - \mu_k)^T \right) / N_k \end{cases} \quad (6)$$

where $\gamma(i, k)$ is the posterior probability. Figure 6 illustrates the process of data acquisition and modeling for the stylus tip. For each of the holes in the side of the phantom, the stylus tip is B-scan imaged and its bright echo is semi-automatically segmented. Meanwhile, the spatial position of the stylus tip is tracked. The pixel location of the stylus tip is tracked by the CAMSHIFT method. The ICP-based solution is adopted to solve the probe calibration equation.

ICP-based minimization

Once the two corresponding data sets are obtained, we expect to find a solution for the probe calibration by mapping one set to the other. This problem can be formulated as follows: let $p_{I,i}$ be the pixel location of feature point in the B-scan image coordinate I and $p_{W,j}$ be the spatial position of the stylus tip within the 3-D

world coordinate system W . Given the two point sets, $X = \{p_{I,i}, i \in [1, N]\}$ and $Y = \{p_{W,j}, j \in [1, M]\}$, we aim to find an optimal transformation $T_{I \rightarrow S}$ that represents the spatial correspondence from the B-scan image coordinate I to the sensor coordinate S . Based on $T_{I \rightarrow S}$, each pixel in the B-scan image can be transferred into the 3-D world space. Therefore, these B-scan slices can be used to reconstruct into a volume.

The two corresponding point sets are related by the eqn (2), which is often solved by minimizing a least-squares error. However, the least-squares minimization assumes that the correspondence between the two point sets X and Y are known. This is usually not the case for our collected data sets, where in general $N \neq M$. Therefore, we introduce the ICP algorithm (Besl and McKay 1992) to best match the two point sets in this report. The advantage of the ICP algorithm is that it does not require the correspondences between X and Y . Alternatively, if the transformation is known, it can be used to estimate the corresponding points. The ICP algorithm iteratively minimizes the following two equations:

$$c_i^k = \min_{p_{W,j} \in Y} |T^k(p_{I,i}) - p_{W,j}|^2 \quad (7)$$

$$T^{k+1} = \min_T |T^k(p_{I,i}) - c_i^k|^2 \quad (8)$$

The ICP algorithm consists of two steps: the correspondence estimation step for eqn (7) and the transformation estimation step for eqn (8). In the correspondence estimation step, we transform each point $p_{I,i} \in X$, using the current estimate of the transformation T^k . Then we look for the point in Y that is closest to $T^k(p_{I,i})$. This point is labeled as the corresponding point c_i^k at iteration k . The result of this step is a set of pairs of corresponding points $\{p_{I,i}, c_i^k\}$. In the transformation estimation step, we look for the transformation that best describes this set of correspondence. Once a better transformation T^k is estimated, we can use it to make a better set of correspondence and so on, until convergence. If the spatial position of two point sets are apart by a good amount, the ICP-based solution may fail to match point clouds.

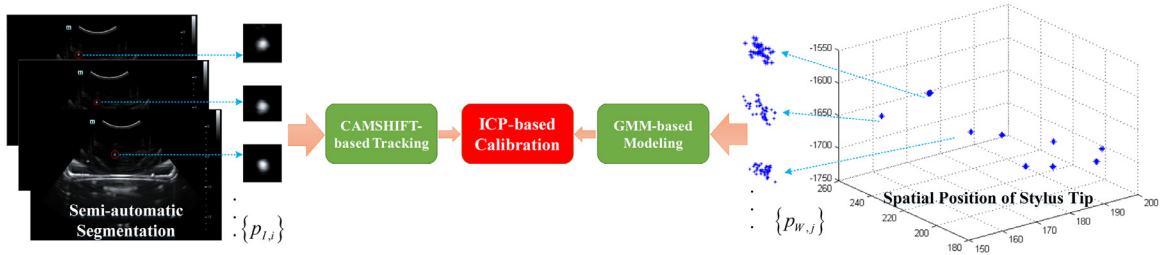


Fig. 6. The process of data acquisition and modeling for stylus tip. For each of the holes in the side of the phantom, the stylus tip is B-scan imaged and its bright echo is semi-automatically segmented. Meanwhile, the spatial position of the stylus tip is tracked. The pixel location of the stylus tip is tracked by the CAMSHIFT method. The ICP-based solution is adopted to solve the probe calibration equation.

Algorithm 1. ICP-based optimization

Input: Two point sets $X = \{p_{l,i}, i \in [1, N]\}$ and $Y = \{p_{w,j}, j \in [1, M]\}$
Output: The transformation matrix $T_{l \rightarrow s}$
Auxiliary functions:
 function for computing the mean of the point set Y using GMM: $\mu_i = \text{GMM}(Y)$
 function for finding the closest point in Y point set: $c_i = \text{Locator}(y_i)$
 function for computing the intermediate transformation of the pairs of corresponding points using closed form solution (CFS): $T = \text{CFS}(\{p_{l,i}, c_i\})$

Begin
 1: $k = 0; \varepsilon = 0.01;$
 2: $c_i^k := \mu_i = \text{GMM}(Y);$
 3: $\text{Locator}()$: Build with point set $Y;$
 4: $T^k = \text{CFS}(\{p_{l,i}, c_i^k\});$
 5: **do** $\{\text{// the transformation step}$
 6: **do** $\{\text{// the correspondence step}$
 7: $y_i = T^k(p_{l,i});$
 8: $c_i^k = \text{Locator}(y_i);$
 9: **while** $(i < \text{NumberOfLandmarks})$
 10: $T^{k+1} = \text{CFS}(\{p_{l,i}, c_i^k\});$
 11: **while** $(k < \text{MaxNumberOfIterations} \text{ // } \|T^{k+1}(p_{l,i}) - c_i^k\|_2 < \varepsilon)$
 12: $T_{l \rightarrow s} = T^k.$
End

For this, we initialize the ICP algorithm with the estimated transformation from the following CAD model:

The pseudo code of the ICP-based calibration algorithm is summarized in Algorithm 1. The codes in lines 1–4 are used to initialize the ICP algorithm. The spatial position data of the stylus tip is modeled by the GMM method in line 2, according to eqn (5) and used to build the k -dimensional tree-based search object (*i.e.*, *Locator*), which makes the complex search problem trivial, in line 3. Then we make the initial transformation estimation $T^k = 0$, using the closed form solution. Based on the T^k , each pixel location $p_{l,i} \in X$ of the feature point is transformed in lines 7 and further used to find its correspondence $c_i^k \in Y$ in line 8. Once the correspondence between two point sets X and $\{c_i^k\}$ is found, we make the transformation estimation based on the closed form solution, in line 10. The ICP-based algorithm does not end until the maximum distance between $T^{k+1}(p_{l,i})$ and c_i^k is below the tolerance threshold ε or until the maximum iteration number is reached.

From the description of the ICP, this optimization method has superior robustness to probe calibration. First, it does not require the exact temporal matching for the data acquisition of the two point sets, X of the B-scan image and Y of the stylus tip, because it can automatically find the correspondence for the two point sets. Second, the acquired data can be modeled with a more robust method such as the GMM, because the ICP does not assume the correspondences between X and Y . Once the probe is calibrated, the B-scan image is spatially

positioned in the 3-D world coordinate system. The targeting region is freehand scanned by the tracked US probe, and the B-scan images with its corresponding positions are collected in the freehand 3-D US imaging system.

RESULTS

Evaluation for probe calibration

To evaluate the calibration accuracy of the probe, we used various positional holes on the side wall of the phantom. The positioning stylus was inserted into the hole consecutively. Its tip was B-scan imaged and semi-automatically tracked by the CAMSHIFT algorithm to output the accurate pixel location continuously. A total of 8 positional holes were selected in our experiment. For each hole, the spatial position data of the stylus tip and its corresponding pixel location were collected continuously for a different period of time (*e.g.*, 1 s, 2 s). Depending on the acquisition time, we collected 8, 40, 80, 160, 240, 320, 480 and 640 data points, respectively. Note that the first group data (*i.e.*, 8) was a one-to-one correspondence for the stylus tip between its pixel location and spatial position. And the proposed ICP-based minimization method was reduced to that of the least-squares method (Rousseau et al. 2003). For the other number of point sets, the proposed ICP-based method was used to solve the spatial transformation for US probe calibration. The index of point reconstruction accuracy (PRA) is used to estimate the calibration accuracy and was defined as follows:

$$\text{PRA} = \|y_i - T \cdot x_i\| \quad (9)$$

where x_i is the pixel location of the stylus tip in the B-scan image, y_i is the spatial position of the stylus tip and T is the estimated spatial transformation. To simulate the transmission of US in the tissue, the water temperature in the water tank was set to approximately 37°C and the imaging depth is set to the phantom depth, (*i.e.*, 100 mm in the experiment).

Table 1 presents the PRA values (mean and standard deviation [SD]) obtained for various numbers of data points. It shows that high accuracy can be achieved by collecting a period of 2 s (80 data points) for each placement of the stylus tip. In addition, the calibration

Table 1. Mean accuracy comparison for various numbers of points*

Number of points	8	40	80	160	240	320	480	640
Mean	1.86	0.86	0.61	0.60	0.60	0.60	0.60	0.60
SD	1.04	0.41	0.21	0.21	0.21	0.21	0.21	0.21

* In millimeters.

Table 2. Convergence comparison under various iterations at the imaging depth of 100 mm*

Iteration	1	2	3	4	5	6
Mean	1.86	1.06	0.60	0.60	0.60	0.60
SD	1.04	0.82	0.21	0.21	0.21	0.21

* In millimeters.

Table 3. Measurement of calibration time* and PRA accuracy†

Volunteers	First round		Second round	
	Time	Accuracy	Time	Accuracy
A	4'67''	0.70	1'39''	0.65
B	4'82''	0.64	1'46''	0.68

* In minutes plus seconds.

† In millimeters.

error of the proposed method is much lower than that of the least-squares minimization method.

To evaluate the convergence of the ICP-based calibration algorithm, Table 2 presents the probe calibration error under various iteration numbers. It is observed that the calibration error drops rapidly as the iteration increases. The proposed algorithm converges quickly after 3 iterations.

To assess the feasibility of the calibration process, 2 physician volunteers, with minimal training, were asked to perform the probe calibration for the first round. Once they gained the calibration experience, the physician volunteers were asked to repeat the calibration procedure for the second round. The operation time and the calibration accuracy were recorded and compared between the two operations, as presented in Table 3. The operation time and calibration accuracy were similar for the two volunteers. It takes less than 5 min for both volunteers to complete the calibration procedure for the first round. Once they gained experience, the operation time was

reduced to less than 1.5 min for the second round. In the experiment, most of the operation time was spent on the manual switching for stylus insertion. Meanwhile, we observed that the calibration accuracy did not show an obvious difference between the 2 operations.

Evaluation for reconstruction accuracy

Similar to the evaluation method of Kim *et al.* (2013), the accuracy of the probe calibration is further verified by 3-D imaging—a string mockup with known geometry—and comparing the reconstructed volume image with its CAD model, as shown in Figure 7a. The mockup consists of 14 strings (made of $\Phi 0.69$ -mm badminton line), forming a 7×7 orthogonal grid with 20-mm \times 20-mm spacing (Fig. 7b). The mockup was submerged in a water tank and the custom-designed software (Wen *et al.* 2018) was used for scanning the strings and 3-D image reconstruction (Fig. 7c). The volume data were then segmented by thresholding the strings in the center imaging region (*i.e.*, 3×5 grids) were fitted with the line model (Fig. 7d). With the fitted strings, the angle between all pairs of strings and the distance between all pairs of intersection points from the image and the CAD model were compared. In our experiment, there were C_2^8 angles between the pairs of strings measured from the acquired image, and the accuracy of the reconstructed angle was $0.28^\circ \pm 0.20^\circ$. Similarly, there were C_2^{15} distance between the pairs of intersection points measured from the acquired image, and the accuracy of the reconstructed distance was 0.40 ± 0.23 mm.

DISCUSSION AND CONCLUSIONS

In this report, we propose an easy-to-use and accurate probe calibration approach to create freehand 3-D US images for image-guided surgical procedures. First, a novel calibration phantom combined with the tracking

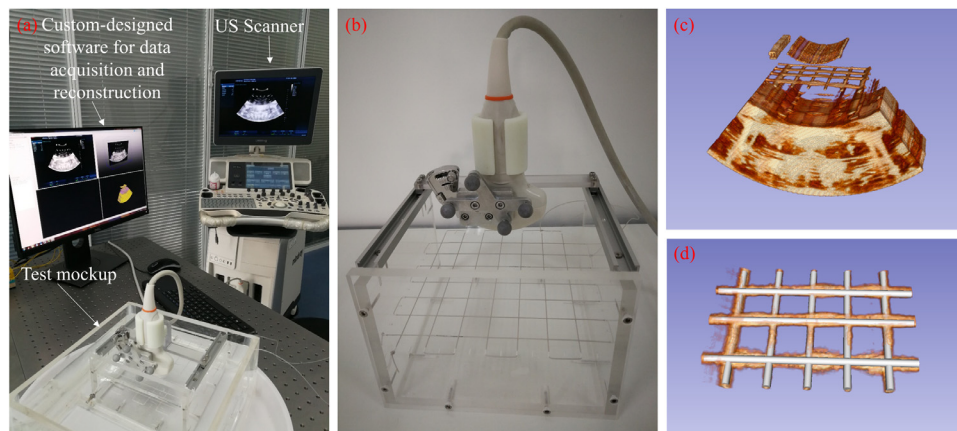


Fig. 7. Probe calibration accuracy measurement. (a) Experimental setup. (b) The test mockup. (c) 3-D US image of the test mockup. (d) Fitted strings and angle and distance measurement.

Table 4. Mean accuracy comparison among various calibration methods*

Method	Cross-wire (Hsu et al. 2008)	Cross-wire (Melvær et al. 2012)	N-wire (Carbajal et al. 2013)	Wall Phantom (Najafi et al. 2015)	This report
Mean	1.5	3.7	1.40	0.86	0.71
SD	—†	2.3	2.0	0.28	0.21

* In millimeters.

† Indicates the missing data.

stylus is proposed to simplify the probe calibration procedure by imaging the stylus tip directly. To obtain the exact pixel location of the stylus tip in the B-scan image, a CAMSHIFT-based algorithm is proposed for the semi-automatic extraction and real-time tracking. Meanwhile, the spatial position of the stylus tip is confirmed and modeled with the GMM method. With the two corresponding point sets, the ICP-based algorithm is used to solve the probe calibration equation. Experimental results demonstrate that the probe calibration method achieves a 0.60-mm mean PRA accuracy and provides the user with a quick, accurate and reliable calibration framework. The validation experiments based on the test mockup with known geometry demonstrates a 0.28° angle accuracy and 0.40-mm distance accuracy, respectively. The acquired B-scan images are reconstructed into a target volume with high accuracy. However, the reconstruction accuracy of 3-D US imaging may be affected by the tissue movement *in vivo*, like respiration or heart beats in cardiology. Tissue movement is not considered for the evaluation of reconstruction accuracy. It is a challenge to eliminate the tissue movement when we perform freehand 3-D US imaging.

The probe calibration accuracy obtained for our method and the other state-of-art calibration methods are compared and presented in Table 4, which demonstrates that the proposed calibration method achieves a lower mean and SD scores than the other comparable methods. Hsu et al. (2008) achieved an internal accuracy of approximately 1.5 mm at a depth of 15 cm. Melvær et al. (2012) achieved an internal accuracy of 3.7 ± 2.3 mm at a depth of 14 cm. Hsu et al. (2008) used an optical tracking system, which, in general, has better accuracy than the electromagnetic tracking systems in Melvær et al.'s (2012) method. Carbajal et al. (2013) achieved a mean accuracy of 1.40 ± 2.0 mm at a depth of 15 cm. Najafi et al. (2015) achieved a mean accuracy of 0.86 ± 0.28 mm at a depth range of approximately 40 mm. We achieved a mean accuracy of 0.71 ± 0.21 under the various depth settings in our experiment. From this experiment, the proposed method outperforms under the PRA evaluation index and is competitive compared with the other well-reported methods.

Ideally, there would be only one point location reading for each of the holes in the side of the phantom.

However, there are slight variations for each stylus insertion because of the position error caused by the tracking system and manual operation for each stylus insertion. Accordingly, we collected a group of data points for each hole and a point cloud solution is adopted in our method. Except for the spatial position of stylus tip, the calibration accuracy depends on the how well the echo spot of the stylus tip can be located in the phantom and detected in the B-scan image. The identification of stylus tip in the B-scan image by manual selection is prone to errors attributable to the operator's variability. On the other hand, fully automatic detection may increase the complexity of the method. The semi-automatic method only requires the user to draw a circle around the bright echo spot of the feature point, then it is able to automatically track the feature spot and output the mean 2-D pixel location. Such a feature detection method would be easy to manipulate even for an inexperienced user.

One potential limitation of the proposed solution is the numerical ill conditioning, which is that small changes in the data may cause arbitrarily large changes in the results. Although there is no numerical ill conditioning in our experiment, it does not mean that this situation will not happen. For the ill-posed conditioning, the data may be analyzed by various regularization methods, including truncated least squares, regularized least squares and truncated total least squares (Fierro et al. 1997).

It is a challenge to manage the speed-of-sound issues when the probe calibration is performed. The speed of sound depends on the medium and its temperature. The speed of sound assumed by most US machines is the average speed of sound in human tissue. Our solution is to increase the temperature of water to the normal temperature of human tissue. Note that the water temperature in the experiment may not be high enough to create the fully matching speed of sound used by the US imager, but the PRA would be within 1 mm according to Sato et al.'s (1998) work. There are alternative approaches to manage the speed of sound of the medium, such as adding salt to the water in the correct percentage (Leotta et al. 1997b) and compensating for the measured point locations in the US image (Mercier et al. 2005).

Acknowledgments—This study was financed partially by the National Natural Science Foundation of China (No. 81827805, 61401451), the National Key R&D Program of China (No. 2018 YFA0704102), the Key Laboratory of Health Informatics in Chinese Academy of Sciences and the Shenzhen Engineering Laboratory for Key Technology on Intervention Diagnosis and Treatment Integration. The authors would like to thank the anonymous reviewers for their fruitful comments.

conflict of interest—The authors declare they have no competing interests.

SUPPLEMENTARY MATERIALS

Supplementary material associated with this article can be found in the online version at doi:[10.1016/j.ultrasmedbio.2020.03.018](https://doi.org/10.1016/j.ultrasmedbio.2020.03.018).

REFERENCES

- Besl PJ, McKay ND. A method for registration of 3-D shapes. *IEEE Trans Pattern Anal Mach Intell* 1992;14:239–256.
- Bouchet LG, Meeks SL, Goodchild G, Bova FJ, Buatti JM, Friedman WA. Calibration of three dimensional ultrasound images for image-guided radiation therapy. *Phys Med Biol* 2001;46:559–577.
- Bradski GR, Clara S. Computer vision face tracking for use in a perceptual user interface. In: *Proceedings of the Fourth IEEE Workshop on Applications of Computer Vision (WACV'98)*. Piscataway, NJ: IEEE; 1998. p. 214–219.
- Carbajal J, Lasso A, Gómez Á, Fichtinger G. Improving N-wire phantom-based freehand ultrasound calibration. *Int J Comput Assist Radiol Surg* 2013;8:1063–1072.
- Fenster A., Bax J., Neshat H., Kakani N., Romagnoli C. 3-D ultrasound imaging in image-guided intervention, in *Advancements and breakthroughs in ultrasound imaging* (chapter 1), published online in *InTech*, 2013. <https://www.intechopen.com/books/advancements-and-breakthroughs-in-ultrasound-imaging/3d-ultrasound-imaging-in-image-guided-intervention>. Accessed by 6 November 2013.
- Fierro RD, Golub GH, Hansen PC, O'Leary DP. Regularization by truncated total least squares. *SIAM J Sci Comput* 1997;18:1223–1241.
- Fukunaga K, Hostetler L. The estimation of the gradient of a density function, with applications in pattern recognition. *IEEE Trans Inf Theory* 1975;21:32–40.
- Hsu PW, Prager RW, Gee AH, Treece GM. Freehand 3-D ultrasound calibration: A review. In: *Sensen CW, Hallgrímsson B, (eds). Advanced imaging in biology and medicine*. Berlin/Heidelberg: Springer; 2009.
- Hsu PW, Treece GM, Prager RW, Houghton NE, Gee AH. Comparison of freehand 3-D ultrasound calibration techniques using a stylus. *Ultrasound Med Biol* 2008;34:1610–1621.
- Khamene A, Sauer F. A novel phantom-less spatial and temporal ultrasound calibration method. *Medical image computing and computer-assisted intervention-MICCAI 2005*. Berlin/Heidelberg: Springer; 2005. p. 65–72.
- Kim C, Chang D, Petrisor D, Chirikjian G, Han M, Stoianovici D. Ultrasound probe and needle-guide calibration for robotic ultrasound scanning and needle targeting. *IEEE Trans Biomed Eng* 2013;60:1728–1734.
- Kowal J, Amstutz CA, Caversaccio M, Nolte LP. On the development and comparative evaluation of an ultrasound B-mode probe calibration method. *Comput Aided Surg* 2003;8:107–119.
- Leotta DF. An efficient calibration method for freehand 3-D ultrasound imaging systems. *Ultrasound Med Biol* 2004;30:999–1008.
- Leotta DF, Detmer PR, Martin RW. Performance of a miniature magnetic position sensor for three-dimensional ultrasound imaging. *Ultrasound Med Biol* 1997;23:597–609.
- Leotta DF, Munt B, Bolson EL, Martin RW, Kraft C, Otto CM, Sheehan FH. Quantitative three-dimensional echocardiography by rapid imaging from multiple transthoracic windows: *In vitro* validation and initial *in vivo* studies. *J Am Soc Echocardiogr* 1997;10:830–839.
- Lindseth F, Tangen GA, Langø T, Bang J. Probe calibration for freehand 3-D ultrasound. *Ultrasound Med Biol* 2003;29:1607–1623.
- Meairs S, Beyer J, Hennerici M. Reconstruction and visualization of irregularly sampled three- and four-dimensional ultrasound data for cerebrovascular applications. *Ultrasound Med Biol* 2000;26:263–272.
- Melvær EL, Mørken K, Samset E. A motion constrained cross-wire phantom for tracked 2-D ultrasound calibration. *Int J Comput Assist Radiol Surg* 2012;7:611–620.
- Mercier L, Langø T, Lindseth F, Collins D. A review of calibration techniques for freehand 3-D ultrasound systems. *Ultrasound Med Biol* 2005;31:449–471.
- Moré JJ. The Levenberg-Marquardt algorithm: Implementation and theory. In: *Watson GA, (ed). Numerical analysis. Lecture notes in mathematics*. 630, Berlin/Heidelberg: Springer; 1978. p. 105–116.
- Mozaffari MH, Lee WS. Freehand 3-D ultrasound imaging: A systematic review. *Ultrasound in Medicine & Biology* 2017;43:2099–2124.
- Muratore DM, Galloway RL. Beam calibration without a phantom for creating a 3-D freehand ultrasound system. *Ultrasound Medicine & Biology* 2001;27:1557–1566.
- Najafi M, Afsham N, Abolmaesumi P, Rohling R. A closed-form differential formulation for ultrasound spatial calibration: Multi-wedge phantom. *Ultrasound Med Biol* 2014;40:2231–2243.
- Najafi M, Afsham N, Abolmaesumi P, Rohling R. A closed-form differential formulation for ultrasound spatial calibration: Single wall phantom. *Ultrasound Med Biol* 2015;41:1079–1094.
- Nelson TR, Pretorius DH. Interactive acquisition, analysis and visualization of sonographic volume data. *Int J Imag Syst Technol* 1997;8:26–37.
- Prager RW, Rohling R, Gee A. Rapid calibration for 3-D freehand ultrasound systems. *Ultrasound Med Biol* 1998;24:855–869.
- Rousseau F, Hellier P, Barillot C. Robust and automatic calibration method for 3-D freehand ultrasound. *Medical image computing and computer-assisted intervention-MICCAI 2003*. Berlin/Heidelberg: Springer; 2003. p. 440–448.
- Rousseau F, Hellier P, Barillot C. Confusius: A robust and fully automatic calibration method for 3-D freehand ultrasound. *Med Image Anal* 2005;9:25–38.
- Sato Y, Nakamoto M, Tamaki Y, Sasama T, Sakita I, Nakajima Y, Monden M, Tamura S. Image guidance of breast cancer surgery using 3-D ultrasound images and augmented reality visualization. *IEEE Trans Med Imaging* 1998;17:681–693.
- Welch JN, Bax M, Mori K, Krummel T, Shahidi R, Maurer CR. A fast and accurate method of ultrasound probe calibration for image-guided surgery. In: *Lemke HU, Inamura K, Doi K, Vannier MW, Farman AG, Reiber JHC, (eds). Computer assisted radiology and surgery-CARS 2002*. Berlin/Heidelberg: Springer; 2002. p. 1078.
- Wen TX, Yang F, Gu J, Chen SF, Wang L, Xie YQ. An adaptive kernel regression method for 3-D ultrasound reconstruction using speckle prior and parallel GPU implementation. *Neurocomputing* 2018;275:208–223.
- Xiao Y, Fortin M, Unsgård G, Rivaz H, Reinertsen I. REtrospective Evaluation of Cerebral Tumors (RESECT): A clinical database of pre-operative MRI and intra-operative ultrasound in low-grade glioma surgeries. *Med Phys* 2017;44:3875–3882.
- Zhang H, Cheng A, Kim Y, Ma Q, Chirikjian G, Bector E. Phantom with multiple active points for ultrasound calibration. *Journal of Medical Imaging* 2018;5(4). doi: 10.1117/1.JMI.5.4.045001.